PAPER

Check for updates

Construction of a binary S-scheme S-g-C₃N₄/Co-ZF heterojunction with enhanced spatial charge separation for sunlight-driven photocatalytic performance†

Ali Bahadur,[a] Shahid Iqbal, [ID] *[b] Mohsin Javed,[c] Syeda Saba Hassan,[c] Sohail Nadeem,[c] Ali Akbar, [ID] [d] Rami M. Alzhrani,[e] Murefah Mana Al-Anazy, [ID] [f] Eslam B. Elkaeed, [ID] [g] Nasser S. Awwad,[h] Hala A. Ibrahium[ij] and Ayesha Mohyuddin[c]

A step-scheme (S-scheme) photocatalyst made of sulfurized graphitic carbon nitride/cobalt doped zinc ferrite (S-g-C₃N₄/Co-ZF) was constructed using a hydrothermal process because the building of S-scheme systems might increase the lifespan of highly reactive charge carriers. Utilizing cutting-edge methods, the hybrid photocatalyst was evaluated by employing TEM, XPS, XRD, BET, FTIR, transient photo-response, UV-vis, EIS and ESR signals. In order to create a variety of binary nanocomposites (NCs), nanoparticles (NPs) of 6% cobalt doped zinc ferrite (Co-ZF) were mixed with S-g-C₃N₄ at various concentrations, ranging from 10 to 80 wt%. For photocatalytic dye removal, a particular binary NC constructed between S-g-C₃N₄ and Co-ZF produces a huge amount of catalytic active sites. The findings showed that loading of S-g-C₃N₄ on 6% Co-ZF NPs serves as a good heterointerface for e^-/h^+ separation and transportation through the S-scheme S-g-C₃N₄/Co-ZF heterojunction. By boosting the hybrid system's BET surface area for the photocatalytic process, the addition of 6% Co-ZF improves the system's ability to absorb more sunlight and boosts its photocatalytic activity. The highest photo-removal effectiveness (98%), which is around 2.45 times higher than that of its competitors, was achieved by the hybrid photocatalyst system with an ideal loading of 48% Co-ZF. Furthermore, the trapping studies showed that the primary species involved in the MB aqueous photo-degradation were $^\bullet OH^-$ and h^+.

aDepartment of Chemistry, College of Science and Technology, Wenzhou-Kean University, Wenzhou, China

bDepartment of Chemistry, School of Natural Sciences (SNS), National University of Science and Technology (NUST), H-12, Islamabad, 46000, Pakistan. E-mail: shahidiqbal.chem@sns.nust.edu.pk

cDepartment of Chemistry, School of Science, University of Management and Technology, Lahore, Pakistan

dDepartment of Physics, University of Agriculture Faisalabad (UAF), Faisalabad, Punjab, 38000, Pakistan

eDepartment of Pharmaceutics and Industrial Pharmacy, College of Pharmacy, Taif University, P.O. Box 11099, Taif 21944, Saudi Arabia

fDepartment of Chemistry, College of Science, Princess Nourah bint Abdulrahman University, P.O. Box 84428, Riyadh 11671, Saudi Arabia

gDepartment of Pharmaceutical Sciences, College of Pharmacy, AlMaarefa University, Riyadh 13713, Saudi Arabia

hChemistry Department, Faculty of Science, King Khalid University, P.O. Box 9004, Abha 61413, Saudi Arabia

iBiology Department, Faculty of Science, King Khalid University, P.O. Box 9004, Abha 61413, Saudi Arabia

jDepartment of Semi Pilot Plant, Nuclear Materials Authority, P.O. Box 530, El Maadi, Egypt

† Electronic supplementary information (ESI) available. See https://doi.org/10.1039/d1ra08525e

Introduction

The need for clean water sources has spurred interest on a global scale as a result of the world population's ongoing rise as well as the quickening pace of industrialization and urbanization.[1–3] Several textile businesses release byproducts that include water during this fast growth, especially colors like methyl orange (MO) and methylene blue (MB), both of which are very lethal and toxic.[4–6] Mixing dirty water with pure water results in considerable environmental pollution.[7–9] Degrading incompatible organic molecules and purifying the water are therefore important to save the ecology.[10–12] Organic dye molecules are challenging to spontaneously decay due to their bulky and complicated chemical structure.[13–15]

Organic pollutant elimination is a well-established potential of photon-initiated oxidation processes, notably photocatalysis.[16–20] This method's notable benefits include the utilization of inexpensive photons, mild working temperatures, nontoxic photocatalysts, and full mineralization.[21–26] Light absorption, photocatalytic redox interactions with reactive radicals, and the separation and transport of the photogenerated electron–hole pair are generally the three key components of the photocatalytic process.[27–30]

Due to its distinctive qualities, such as environmental friendliness, affordability, a moderate working temperature, and high oxidation power, semiconductor-based photocatalysts have been extensively used to remove environmental contaminants from water.[31–33] It is a drawback because TiO_2 has a significant bandgap (3.22 eV), which implies that only 4% of the solar spectrum is captured and the rest is lost. There have lately been several novel photocatalytic semiconducting materials that destroy organic complex compounds by reacting to visible light. Physiochemical characteristics, non-toxicity, and outstanding photocatalytic efficiency of spinel ferrites have made them popular photocatalysts in environmental cleanup.[34–36] Zinc ferrite ($ZnFe_2O_4$) is a spinel-type (AB_2O_4) material that is stable because $Zn(II)$ ions dominate the tetrahedral A-site and $Fe(III)$ ions reside in the octahedral B-sites.[34] It has been used in several applications because of its optoelectronic qualities, photochemical stability and narrow bandgap (1.9 eV), including magnetic materials, gas sensors, pigment, hydrogen production, solar energy active photocatalyst for the photo-removal of organic pollutants and as an anode material in batteries.[6,37]

There are several ways to make zinc ferrite (ZF), including solvothermal, co-precipitation, hydrothermal, microemulsion, sol–gel, the reverse micelle technique, solid-state processes and combustion.[38,39] Due to its simplicity, ability to produce crystals with the required morphology, size, and form, high productivity, and improved solubility, the hydrothermal process is more often used than other synthetic techniques.[40–42] Additionally, a lot of crystals may be produced using this technique without altering the composition, and materials with high vapor pressure close to their melting point can also be formed. $ZnFe_2O_4$ nanocrystals were created by Fan et al. via a hydrothermal technique, and they were then utilized to degrade acid orange II.[43] In addition, Sun et al. and Han et al. examined the photocatalytic efficiency of $ZnFe_2O_4$ nanoplates and octahedral $ZnFe_2O_4$ produced by hydrothermal techniques against RhB.[44,45] However, because of insufficient e^- and h^+ pair separation and substantial recombination of photoinduced e^-/h^+, the photocatalytic efficiency of zinc ferrite is severely constrained.

As a consequence, many areas are being concentrated on increasing the effectiveness of the photocatalytic procedure, involving expanding the light-harvesting spectrum range and boosting the transfer and separation of photoinduced e^- and h^+ sets.[46–48] The use of 2D layered materials and metal-doping are typical methods for achieving these objectives. Numerous investigations have shown that non-local-conjugated structures in conductive polymers improve charge carrier transport and boost photocatalytic performance. $Co-ZnFe_2O_4$,[49] $ZnFe_2O_4$/g-C_3N_4,[50] $ZnFe_2O_4$/graphene,[51] and $ZnFe_2O_4$/Fe_2O_3 (ref. 52) are cited in earlier papers as materials that have shown exceptional performance in the elimination of contaminants.

The cobalt-doped $ZnFe_2O_4$ (Co-ZF) NPs used in this study have varying percentages of cobalt (2, 4, 6, 8, and 10 wt%) and a 6% cobalt-doped $ZnFe_2O_4$ composite with varying percentages (12, 24, 48, 60, and 80 wt%) of S-g-C_3N_4 photodegraded using these synthetic photocatalysts and a suggested mechanism for MB degradation was made.

Experimental

Materials

Ferric nitrate nonahydrate ($Fe(NO_3)_3 \cdot 9H_2O$, 99% Alfa Aesar), distilled water, $Zn(NO_3)_3 \cdot 6H_2O$, 97% Sinopharm, sodium hydroxide (NaOH, 99% Alfa Aesar), polyethylene glycol (PEG, 97% DAEJUNG), MB ($C_{16}H_{18}ClN_3S$, 99% Simpsons), cobalt nitrate hexahydrate ($Co(NO_3)_2 \cdot 6H_2O$, 97% DAEJUNG) and thiourea (CH_4N_2S, 99% Sinopharm).

Synthesis of $ZnFe_2O_4$ NPs

$ZnFe_2O_4$ NPs were created using the hydrothermal technique. In a nutshell, 2.98 g of $Zn(NO_3)_3 \cdot 6H_2O$ and 8.09 g of $Fe(NO_3)_3 \cdot 9H_2O$ were dissolved in 31 mL of distilled water before being combined with 11 mL of polyethylene glycol (PEG) and rapidly agitated for 22 minutes. To keep the mixture's pH at 11, a dropwise addition of a 7 M NaOH solution was made with constant stirring. For hydrothermal treatment at 182 °C for 17 hours, this suspension was vacuum sealed in a 100 mL Teflon autoclave. The temperature was then raised to the normal range. The item underwent many rounds of filtering and distilled water washings before being dried in the oven for three hours at 85 °C. A fine powder was created once the product was finished.

Synthesis of Co-ZF NPs

By adjusting the cobalt content of $ZnFe_2O_4$ (2, 4, 6, 8, and 10 wt%), cobalt doped $ZnFe_2O_4$ (Co-ZF) NPs were also produced hydrothermally. To make 2% Co-ZF, 0.08 g of $Co(NO_3)_2 \cdot 6H_2O$, 8.09 g of $Fe(NO_3)_3 \cdot 9H_2O$ and 2.91 g of $Zn(NO_3)_3 \cdot 6H_2O$ were dispersed in 31 mL of distilled H_2O. The mixture was then given a further addition of 11 mL of PEG and aggressively agitated for 22 minutes. When the combination's pH reached 11, a dropwise addition of a 7 M solution of NaOH was made while the mixture was continually stirred. For hydrothermal treatment at 182 °C for 17 hours, this suspension was vacuum sealed in a 100 mL Teflon autoclave. Then, it was let cool to room temperature. The precipitates underwent filtration, washing, and three hours of drying at 85 °C. The substance was then milled into a fine powder after drying. The same process was also used to create Co-ZF in a sequence with wt% of 4, 6, 8, and 10. Table 1 lists the different compositions and testing circumstances.

Construction of S-g-C_3N_4

Utilizing thiourea and the thermal polycondensation technique, S-g-C_3N_4 was created. This process included placing thiourea in the crucible and heating it for three hours at a temperature of 555 °C at a pace of 6 °C min^{-1}. After being milled into a fine powder, the resulting yellow color agglomerates were produced.

Designing of S-g-C_3N_4/Co-ZF heterostructures

By combining different amounts (12, 24, 48, 60, and 80 wt%) of S-g-C_3N_4 with Co-ZF, a series of 6% S-g-C_3N_4/Co-ZF NCs were made. Solution A was created by dissolving 8.09 g of

Table 1 Co-ZF NPs' chemical make-up and an evaluation of their photocatalytic potential

S. no.	Doping in wt%	$Co(NO_3)_2 \cdot 6H_2O$ (g)	$Zn(NO_3)_3 \cdot 6H_2O$ (g)	$Fe(NO_3)_3 \cdot 9H_2O$ (g)	pH	MB dye degradation (%)
1	Pure ZF	0	2.99	8.09	11	37
2	2% Co-ZF	0.08	2.91	8.09	11	46
3	4% Co-ZF	0.16	2.83	8.09	11	54
4	6% Co-ZF	0.24	2.75	8.09	11	60
5	8% Co-ZF	0.32	2.67	8.09	11	52
6	10% Co-ZF	0.40	2.59	8.09	11	44

Table 2 The progression of the photocatalytic efficacies of the synthesized heterostructures and their composition

S. no.	Wt% of 6% Co-ZF in NCs	S-g-C_3N_4 (g)	MB dye removal (%)
1	12%	0.26	69
2	24%	0.53	86
3	48%	1.06	98
4	60%	1.32	86
5	80%	1.76	75

$Fe(NO_3)_2 \cdot 9H_2O$, 2.75 g of $Zn(NO_3)_2 \cdot 6H_2O$ and 0.24 g of $Co(NO_3)_2 \cdot 6H_2O$ in 27 mL of distilled water for the synthesis of 12% NCs of S-g-C_3N_4 with 6% Co-ZF. To create solution B, 0.217 g of S-g-C_3N_4 were mixed with 16 mL of distilled water. Following that, solution A and solution B were combined, and 11 mL of PEG were added. This process took place while the mixture was vigorously stirred for 22 minutes. The pH was

raised to 11 by adding the 7 M solution of NaOH dropwise while stirring the mixture continuously. In a Teflon autoclave, the suspension was moved, and it was heated for 17 hours at 182 °C. The temperature was then lowered to ambient. The sample underwent three hours of drying at 85 °C after being filtered and many times in distilled water. The item was then crushed into a fine powder when it had dried. The same process was also used to create a series of NCs of S-g-C_3N_4 with 6% Co-ZF (24, 48, 60, and 80 wt%). For their synthesis, Table 2 lists the experimental conditions and S-g-C_3N_4 dosage. On the other hand, the ESI† includes the material characterizations and photocatalytic activity data.

Results and discussion

Fig. 1 shows the crystallinity and structure of S-g-C_3N_4 NSs, 6% Co-ZF, ZF, and 48% S-g-C_3N_4/6% Co-ZF NCs as determined by XRD. The cubic spinal structure of 6% Co-ZF, ZF and 48% S-g-
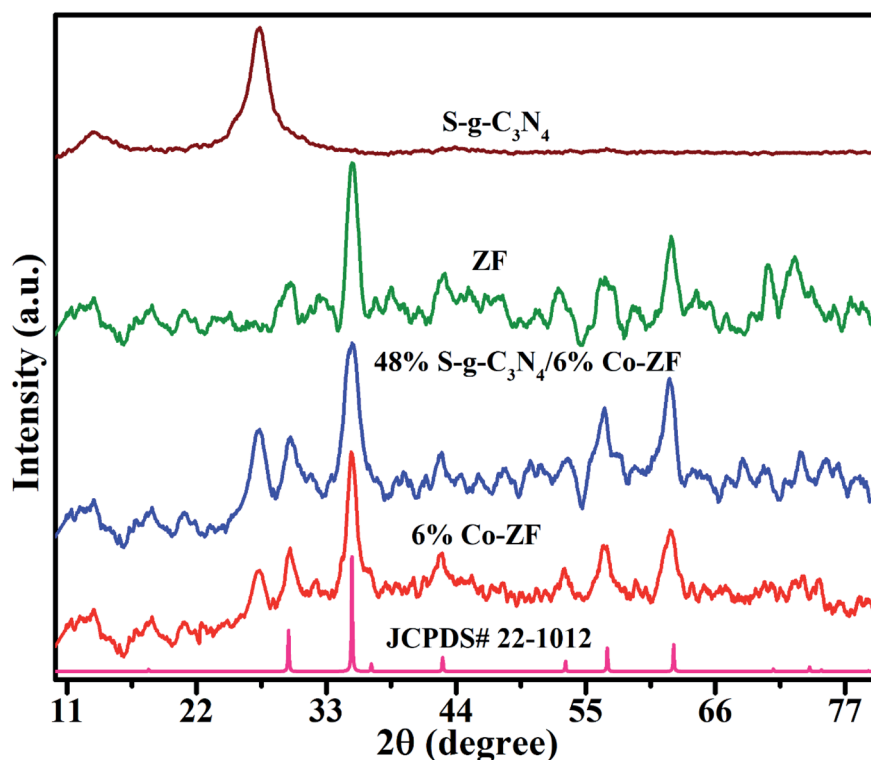
Fig. 1 XRD pattern of zinc ferrite, S-g-C_3N_4, 6% Co-ZF and 48% S-g-C_3N_4/6% Co-ZF.

C_3N_4/6% Co-ZF NCs is shown by their XRD patterns. Fig. 1 shows that the crystalline form of spinal ZF is significantly associated with (JCPDS no. 22.1012) each of the diffraction peaks. The peaks at 2θ of 35.3°, 30.1°, 42.1°, 52.1°, 62.3° and 56.5° are recognized in the (311), (220), (400), (422), (440) and (511) crystal facets of zinc ferrite. The XRD of 6% Co-ZF is also shown in Fig. 1 for your viewing pleasure. Given that cobalt has a smaller ionic radius (0.57 Å) than zinc, the pattern shows that adding 6% of cobalt to ZF marginally enhances the broadness of the peaks (0.59 Å). Therefore, a smaller crystallite results from the replacement of Co in ZF. The rise in peak widening is proof that Co was successfully doped in ZF. The S-g-C_3N_4 diffraction pattern is also seen in Fig. 1. The 002 facets of the crystal are assigned a separate peak in this pattern at 27.37°, and this pattern closely resembles (JCPDS 00-087-1526) the pattern of S-g-C_3N_4 that has been described. The intense peaks in the XRD pattern of 48% S-g-C_3N_4/6% Co-ZF NCs are in strong agreement with the existence of pure ZF. This suggests that adding 48% S-g-C_3N_4 to 6% Co-ZF cannot cause a phase shift, and the fact that there is one peak of SCN at 27.37° indicates that S-g-C_3N_4 was successfully loaded into 6% Co-ZF.

As shown in Fig. 2, TEM images were used to assess the surface morphologies of manufactured photocatalysts in addition to their crystal structures. Curiously, TEM investigation of S-g-C_3N_4 revealed that the produced S-g-C_3N_4 exhibit almost translucent and stretchable 2D homogeneous NSs constructions with bendy shapes (Fig. 2a). Spherical NPs are collected in erratic formations in the ZF TEM picture shown in Fig. 2b, with the size of the particles varying from 22 to 38 nm. This morphology is known as a 0D morphology. However, the Co-ZF with dimensions between 27 and 49 nm was also shown to have a 0D-like shape (Fig. 2c). The TEM picture (Fig. 2d) for the 48% S-g-C_3N_4/6% Co-ZF NCs demonstrates an equal distribution of S-g-C_3N_4 across the Co-ZF NPs. Co-ZF is evenly dispersed as NPs throughout the S-g-C_3N_4 segment, which is really a 2D layered structure. The manufacture of 6% Co-ZF NPs on S-g-C_3N_4 NSs produced the most clearly characterized heterojunction between these two materials.
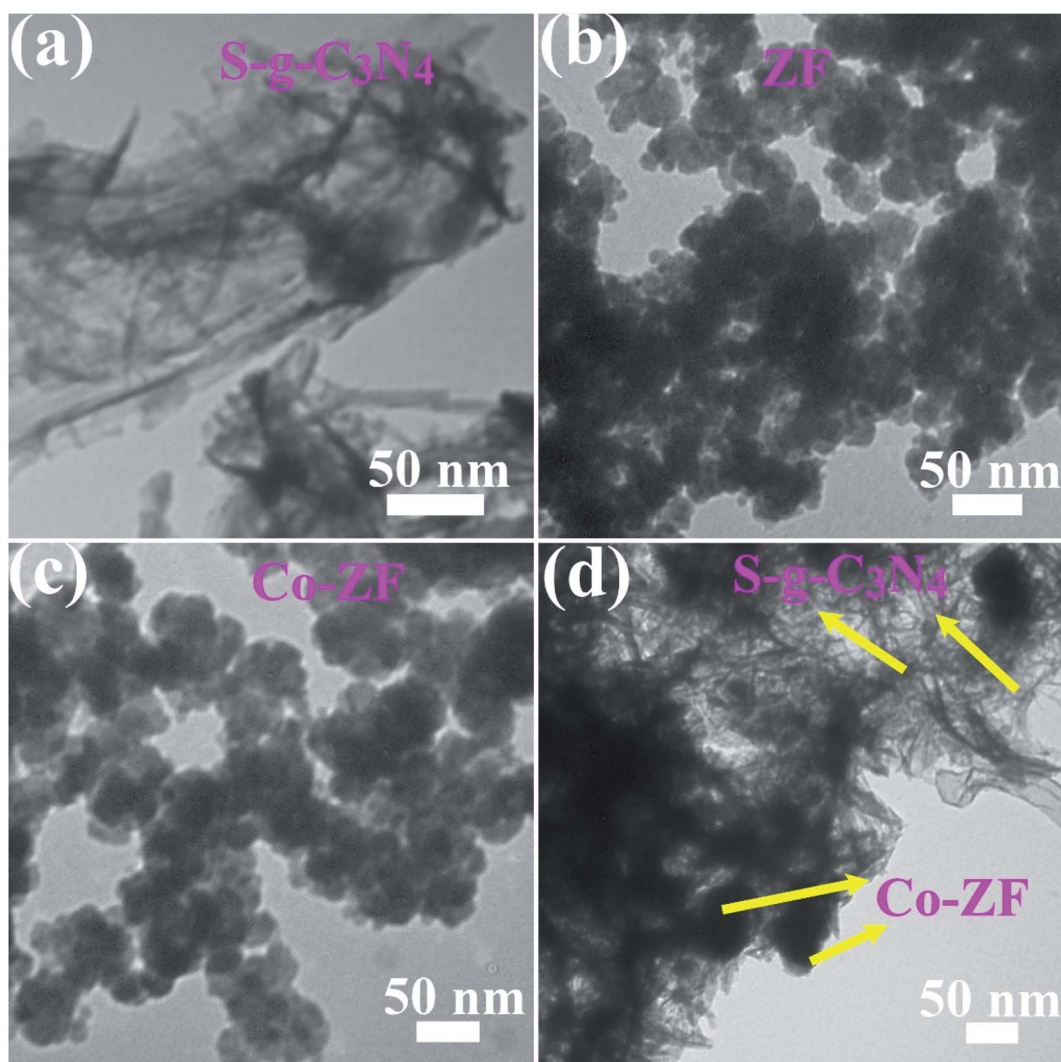

Fig. 2   TEM images of (a) S-g-C_3N_4, (b) ZF, (c) 6% Co-ZF, and (d) 48% S-g-C_3N_4/6% Co-ZF.

Additionally, XPS was used to identify the valence state and elemental conformation and of NCs that were 48% S-g-C_3N_4/6% Co-ZF. According to Fig. S1a,† the Zn $2p_{1/2}$ and Zn $2p_{3/2}$ particles are responsible for the peaks that occurred at 1044.73 eV and 1021.72 eV in the Zn 2p spectra of S-g-C_3N_4/6% Co-ZF.[53,54] Two unique peaks identified at 529.91 and 531.22 eV that may be linked with Fe–O and Zn–O, correspondingly, are validated by the deconvoluted O 1s observations (Fig. S1b†) of S-g-C_3N_4/6% Co-ZF.[55] Two major peaks of the measurements of Fe 2p were used to determine the oxidation states of Fe^{3+} in the synthesized photocatalyst (Fig. S1c†), Fe $2p_{1/2}$ (722.13) and Fe $2p_{3/2}$ (708.43).[56] As shown in Fig. S1d,† the deconvoluted spectra of Co 2p exhibit two distinct peaks that may be assigned to the Co $2p_{1/2}$ and Co $2p_{3/2}$ at BEs of 793.94 and 778.93 eV. The acquired findings are in line with the prior work for the Co-ZF NPs. Three unique peaks seen in the C 1s spectra of S-g-C_3N_4/6% Co-ZF NCs may be assigned to the C–C, C=O, and C–O, individually. These peaks are seen at 283.19, 287.16, and 284.71 eV.[57,58] In Fig. S1e,† the C 1s spectrum is shown. Similarly, three distinct peaks at 397.89, 400.67, and 399.79 eV in the N 1s high-resolution spectra are attributed to the respective N–C–N, N–H, and C–(C)$_3$ functions (Fig. S1f†).[14] The successful synthesis of hybrid S-g-C_3N_4/6% Co-ZF NCs was shown by these XPS experimental results. The XPS findings demonstrated the close contact between Co-ZF and S-g-C_3N_4, resulting in the formation of the nanoscale hybrid system with a content of 48% S-g-C_3N_4 and 6% Co-ZF.

In order to identify the functional group in prepared samples, FTIR spectroscopy is a crucial method. In the 650–4000 cm^{-1} range, FTIR spectroscopy was used to study samples of 6% Co-ZF, ZF, S-g-C_3N_4 and S-g-C_3N_4/6% Co-ZF. Their FTIR spectra are shown in Fig. 3a. The tetrahedral site's M–O bond is responsible for the distinctive peaks in all FTIR spectra that are in the 849–898 nm range. Our ability to observe the M–O bond's peaks at octahedral positions is limited by our instrumentation. Peaks at 842 and 782 cm^{-1} are caused by triazine units, whereas peaks in the area of 1201–702 cm^{-1} are caused by C–N and C=N stretching in the spectra for S-g-C_3N_4 and 48% S-g-C_3N_4/6% Co-ZF.

As shown in Fig. 3b, the isotherms of N_2 desorption–absorption for each of the generated samples of ZF, S-g-C_3N_4, 6% Co-ZF and a 48% S-g-C_3N_4/6% Co-ZF heterostructure are all simulated. The isotherm of a 48% S-g-C_3N_4/6% Co-ZF has been reported to be well suited to mesoporous structures and the standard isotherm pattern of the IUPAC.[59] ZF, S-g-C_3N_4, 6% Co-ZF, and 48% S-g-C_3N_4/6% Co-ZF heterojunction all had BET surface areas computed as 7.98, 29.98, 13.74, and 68.73 $m^2\ g^{-1}$, correspondingly. In comparison to the ZF, S-g-C_3N_4, 6% Co-ZF, and the 48% S-g-C_3N_4/6% Co-ZF have a greater surface area. This is most likely the outcome of the phenomena of
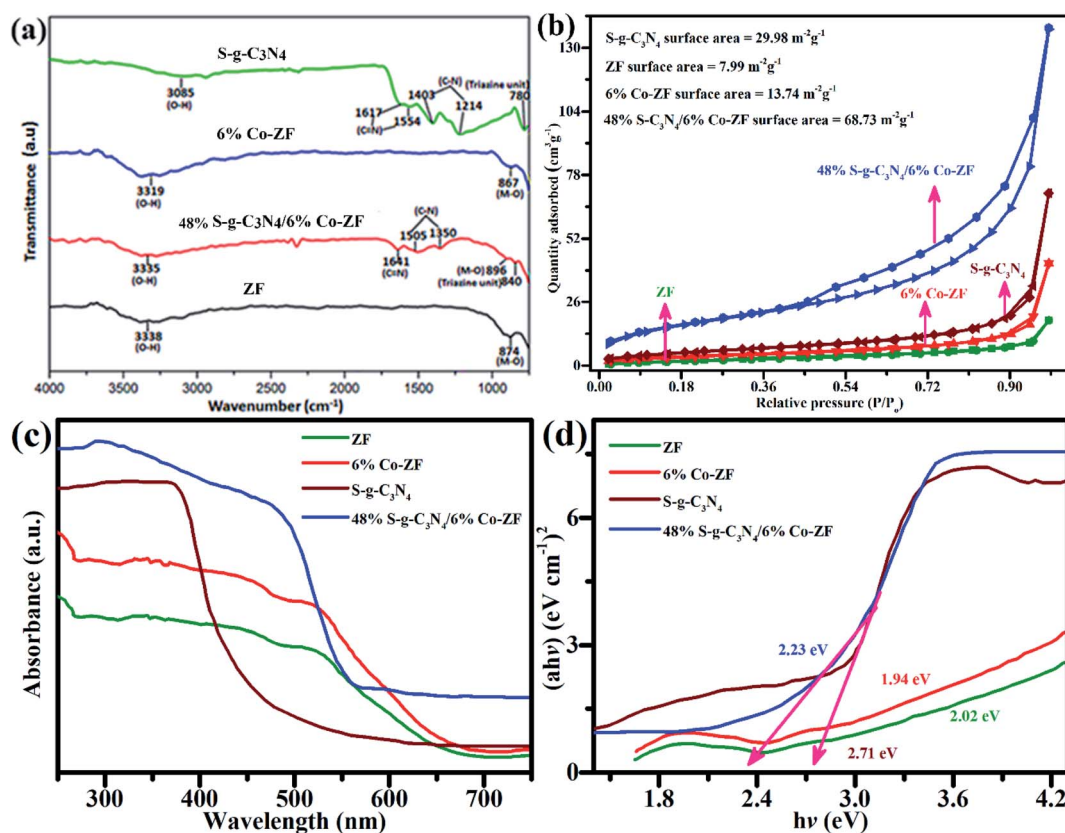

Fig. 3 (a) FT-IR assessments, (b) ZF, S-g-C_3N_4, 6% Co-ZF, and 48% S-g-C_3N_4/6% Co-ZF NCs N_2 adsorption–desorption are used to compute the BET surface area isotherms, (c) UV-vis absorption ranges and (d) Tauc's plots of ZF, S-g-C_3N_4, 6% Co-ZF, and 48% S-g-C_3N_4/6% Co-ZF heterostructure.

arrangement and building of numerous integrated components, which not only promotes the well-defined fabrication but also makes 48% S-g-C$_3$N$_4$/6% Co-ZF more active by generating additional active positions for photocatalysis. High photocatalytic activity is provided by photocatalysts made of 48% S-g-C$_3$N$_4$/6% Co-ZF due to the well-defined manufacturing of heterointerface and enhanced surface area. However, the mesoporous 48% S-g-C$_3$N$_4$/6% Co-ZF exhibits an extraordinary capacity to suppress the photogenerated e$^-$/h$^+$ pairs recombination processes, which subsequently helps to fine-tune the photocatalytic abilities of the 48% S-g-C$_3$N$_4$/6% Co-ZF photocatalyst.

Following that, the light-absorption of the synthesized photocatalysts S-g-C$_3$N$_4$, Co-ZF NPs, ZF NPs and 48% S-g-C$_3$N$_4$/6% Co-ZF were explored by UV-vis spectra. Fig. 3c shows the aggregate collection of UV-vis evaluations with wavelengths between 255 and 755 nm. When the UV-vis measurements of Co-ZF and ZF NPs are compared, a consistent variation in absorption (redshift) is seen. Associating the 48% S-g-C$_3$N$_4$/6% Co-ZF light absorption spectrum to all other samples, including ZF, S-g-C$_3$N$_4$ and Co-ZF NPs spectra, it is notable that the light cultivation is enriched from 255 nm to 755 nm. This increase in absorption is mostly the result of the integration of the 6% Co-ZF with S-g-C$_3$N$_4$, which also contributes to enhancing the photocatalytic efficacies of the heterostructures made up of 48% S-g-C$_3$N$_4$/6% Co-ZF. Additionally, a significant improvement has been made in the light-harvesting capacity in the 505–755 nm region, which is important for photocatalytic efficiency.

By creating the Tauc's plot of the UV-vis measurements, shown in Fig. 3c, the energy bandgap values of these produced photocatalysts were evaluated. The computed bandgap values were found to be 2.02 eV, 1.94 eV, and 2.71 eV for the 6% Co-ZF, ZF and 48% S-g-C$_3$N$_4$/6% Co-ZF, correspondingly, as shown in Fig. 3c. Because cobalt is doped into the ZF NPs, which most likely leads to the creation of new energy regions below the conduction band, the energy bandgap of 6% Co-ZF may be lowered. The sample with a cobalt concentration of 6% had the lowest energy bandgap out of all the designed samples of Co-ZF (2, 4, 8 and 10%). Similar results were obtained when the energy bandgap of the Co-ZF equated to the S-g-C$_3$N$_4$ and the 48% S-g-C$_3$N$_4$/6% Co-ZF fell from 2.71 eV for S-g-C$_3$N$_4$ to 2.23 eV for 48% S-g-C$_3$N$_4$/6% Co-ZF. The effective surface fusion of both components may be to blame for this drop in bandgap values, which significantly increases the photocatalytic abilities of the binary photocatalyst.

Fig. 4 compares the photocatalytic efficiency of a sequence of NCs and ZF with MB. The NCs had Co contents of 2, 4, 6, 8 and 10 wt%. Fig. 4a demonstrates that 6% Co-ZF may degrade MB at a faster rate than other samples, eliminating 60% of it in under 86 min. Later, a nanocomposite of 6% Co-ZF is made with various concentrations of S-g-C$_3$N$_4$ (12, 24, 48, 60 and 80 wt%), and MB degradation is conducted to further improve the photocatalytic efficacy of the nanocomposite. To examine the
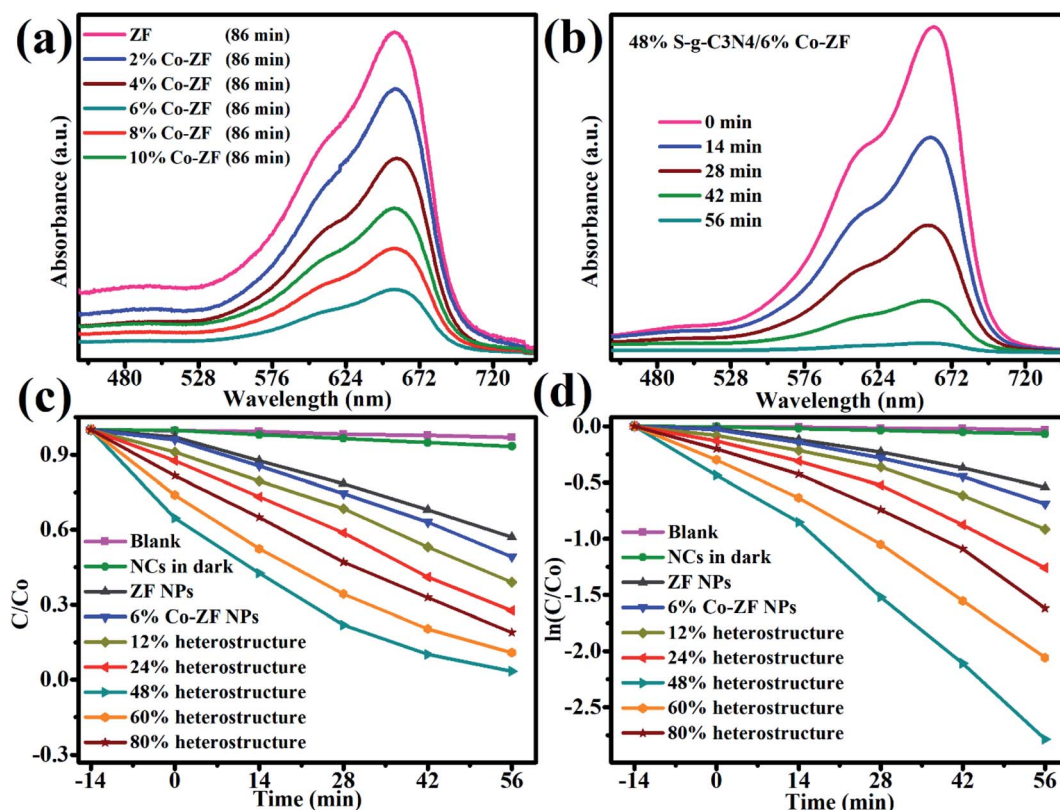

Fig. 4 MB deterioration in visible light illumination measurements for (a) ZF, Co-ZF (2, 4, 6, 8 and 10%) NRs, and (b) 48% S-g-C$_3$N$_4$/6% Co-ZF. (c) MB's photodegradation rate and (d) dye kinetic pseudo-first-order graphs, 6% Co-ZF, ZF, and Co-ZF/S-g-C$_3$N$_4$ (12, 24, 48, 60 & 80 wt%) NCs.

© 2022 The Author(s). Published by the Royal Society of Chemistry

Paper   RSC Advances
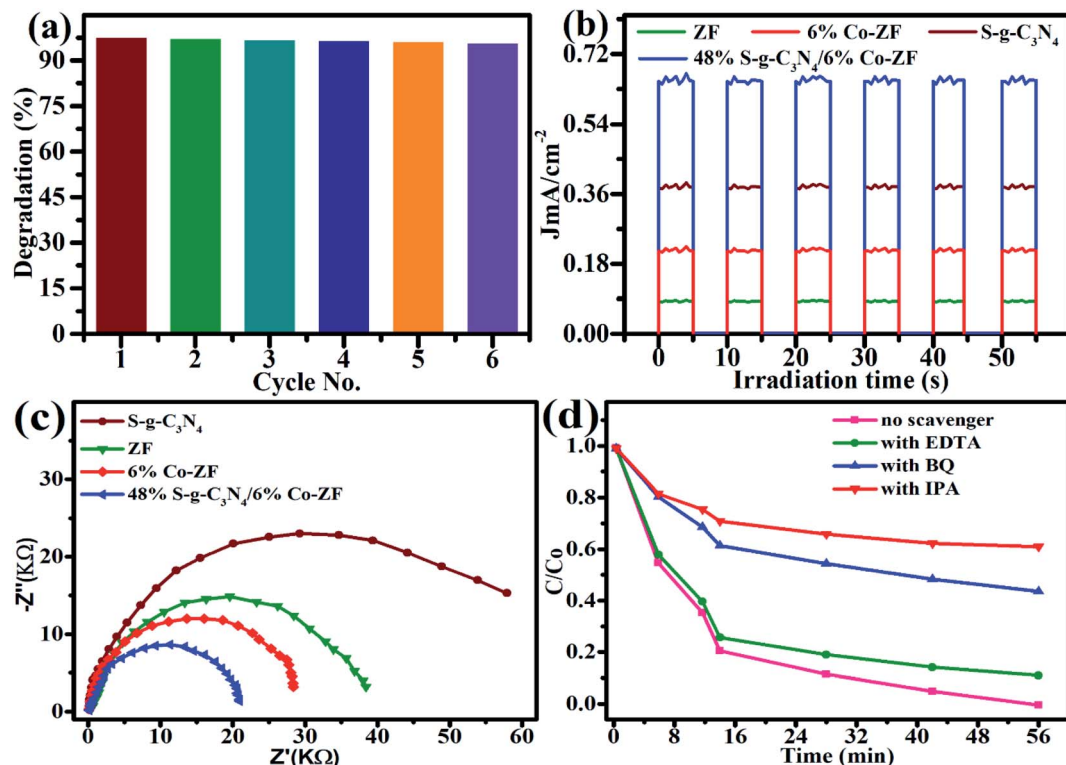
Fig. 5 (a) Cyclic stability of a 48% S-g-C$_3$N$_4$/6% Co-ZF NCs photocatalyst for six subsequent experiments on MB photoremoval. (b) Transient photocurrent results of ZF, 6% Co-ZF, S-g-C$_3$N$_4$, and 48% S-g-C$_3$N$_4$/6% Co-ZF under visible-light irradiation (>420 nm). (c) EIS Nyquist plots of ZF, 6% Co-ZF, S-g-C$_3$N$_4$ and 48% S-g-C$_3$N$_4$/6% Co-ZF NCs. (d) Scavengers' impact on the 48% S-g-C$_3$N$_4$/6% Co-ZF NCs photocatalytic activity.

photocatalytic characteristics of generated NCs with various Co-ZF (12, 24, 48, 60, and 80 wt%) NPs concentrations, visible light illumination of MB was utilized (Fig. 4b). Our investigation of the photodegradation of organic pollutants over a 48% S-g-C$_3$N$_4$/6% Co-ZF revealed that MB degradation may be sped up by raising the Co-ZF content in the 48% S-g-C$_3$N$_4$/6% Co-ZF (Table 2). The highest photodegradation yield of 98% that was observed with this concentration under visible-light irradiation proves that the optimal amount of Co-ZF NPs is 50 wt%. For example, when S-g-C$_3$N$_4$/Co-ZF with 80 wt% of Co-ZF content were used as photocatalysts for MB degradation, the yield was reduced to 75%, suggesting that the yield would be lower with further increasing the Co-ZF NPs content. Even after six-hour runs, the S-g-C$_3$N$_4$/Co-ZF exhibits the highest photodegradation efficiency and chemical stability (Fig. 5a).

Fig. 4c and d illustrate the results of computing the photo-removal rate of dye by photocatalysts using the formula, $\ln\left(\dfrac{C_\mathrm{o}}{C}\right) = Kt$, where C_o and C represent the dye content at zero and t minutes, correspondingly, and K represents the reaction rate. According to this figure, the photo-removal rate of MB is 8.99×10^{-4} min^{-1}. The photolysis rate of 6% Co-ZF (2.58×10^{-3} min^{-1}) is greater than the photocatalysis rate of MB utilizing ZF, which is 1.67×10^{-3} min^{-1} then by creating a composite of 6% Co-ZF and 48% S-g-C$_3$N$_4$, the rate was further elevated and reached 0.42×10^{-3} min^{-1} as a consequence of the synergistic interaction between Co-ZF and S-g-C$_3$N$_4$. Then, it

is shown from estimated results that NCs of 48% S-g-C$_3$N$_4$/6% Co-ZF showed the greatest 98% photo-removal of dye after 56 min, whereas with 6% Co-ZF and ZF the degradation of dye was 60% and 37%, correspondingly. Additionally, as demonstrated in Table 3, 48% S-g-C$_3$N$_4$/6% Co-ZF photocatalytic efficiency is practically greater than that of past studies.

Since it is generally known that the chemical constancy is a key factor in a catalyst's ability to be extensively utilized, the 48% S-g-C$_3$N$_4$/6% Co-ZF heterostructures that were created were assessed for their potential to be employed up to six times in the reaction of dye photo-removal under solar light. The catalyst's impressive chemical stability and availability for routine experimental usage were shown by the fact that there was no visible decline in its efficiency even after 6 runs (Fig. 5a). Photocurrent studies have been performed with all of the available catalysts to dive further into the underlying factors that contribute to the exceptional photocatalytic efficacy of 48% S-g-C$_3$N$_4$/6% Co-ZF for the MB mineralization. This is accomplished by creating a proportional association of photocurrent responses for 48% S-g-C$_3$N$_4$/6% Co-ZF, along with all other catalysts ZF NPs, S-g-C$_3$N$_4$, and 6% Co-ZF NPs, which provides a useful perspective on the transportation of photogenerated electron/hole pairs. The photocurrent response for 6% Co-ZF, ZF, S-g-C$_3$N$_4$, and 48% S-g-C$_3$N$_4$/6% Co-ZF was explored in a 0.5 M Na$_2$SO$_4$ solution under chopping radiance (Fig. 5b). The photocurrent response of the 48% S-g-C$_3$N$_4$/6% Co-ZF was by far the greatest when compared to all other produced catalysts,

Table 3 48% S-g-C$_3$N$_4$/6% Co-ZF photocatalytic effectiveness is compared to that of various previously reported photocatalysts

S. no.	Photocatalyst	Dyes	Light source	Irradiation time (min)	% degradation	Ref.
1	Zn$_{1-x}$Dy$_x$Fe$_2$O$_4$	MB	Mercury lamp	75	97.3	34
2	ZnFe$_2$O$_4$	MB	Xenon lamp	141	76.2	60
3	CeO$_2$/ZnFe$_2$O$_4$	MB	Sunlight	60	90.48	31
4	ZF–RGO	Fulvic acid	Solar light	220	80.1	61
5	rGO/ZnFe$_2$O$_4$	MB	Sunlight	180	99.8	62
6	SnFe$_2$O$_4$/ZnFe$_2$O$_4$	MB	Visible light	120	93.2	63
7	ZnFe$_2$O$_4$/rGO	MB	Visible light	121	99.99	64
8	ZnFe$_2$O$_4$@rGO	MB	Xenon lamp	142	92.5	60
9	ZnFe$_2$O$_4$/Ag/AgBr	RhB	Visible light	80	88	65
10	S-g-C$_3$N$_4$/Co-ZF	MB	Sunlight	56	98	Present work

demonstrating once again how effectively charges are transferred and consumed in the binary catalyst. On the other hand, high photocurrent responses provided well-defined heterointerfaces, excellent electron–hole pair separation, and efficient transfer of electron charge carriers in the very advantageous self-assembled binary 48% S-g-C$_3$N$_4$/6% Co-ZF photocatalytic procedure for dye degradation.

At the electrode–electrolyte junction, an EIS evaluation was recognized in the dark to assess the heterojunction charge transfer rate. The relationship between a shorter arc radius and lowered electron diffusion resistance, faster interfacial photo-generated charge transport, and better exit proficiency is often seen. According to our experimental results (Fig. 5c), the S-g-C$_3$N$_4$/Co-ZF with a 48% S-g-C$_3$N$_4$/6% Co-ZF content had the lowest charge-transmission resistance of all the samples that

were produced. According to this research, the heterointerface contact of the binary heterostructure S-g-C$_3$N$_4$/Co-ZF may greatly promote electron transport and increase electron consumption, enhancing photocatalytic performance. The transitory photocurrent responses and the EIS data accord quite well. According to the aforementioned experimental findings, a well-built S-g-C$_3$N$_4$/Co-ZF might significantly improve light harvesting, quick heterointerface electron transmission, and efficient separation of photoinduced e$^-$–h$^+$ sets.

Additionally, the 48% S-g-C$_3$N$_4$/6% Co-ZF heterostructures may produce a significant number of effective oxygen species that are useful for removing MB from the 48% S-g-C$_3$N$_4$/6% Co-ZF under visible light illumination (Fig. 5d). p-Benzoquinone (BQ), ethylenediaminetetraacetic acid (EDTA), and isopropanol (IPA) were each employed to capture $\cdot$OH, $\cdot$O$_2^-$ and h$^+$ in the
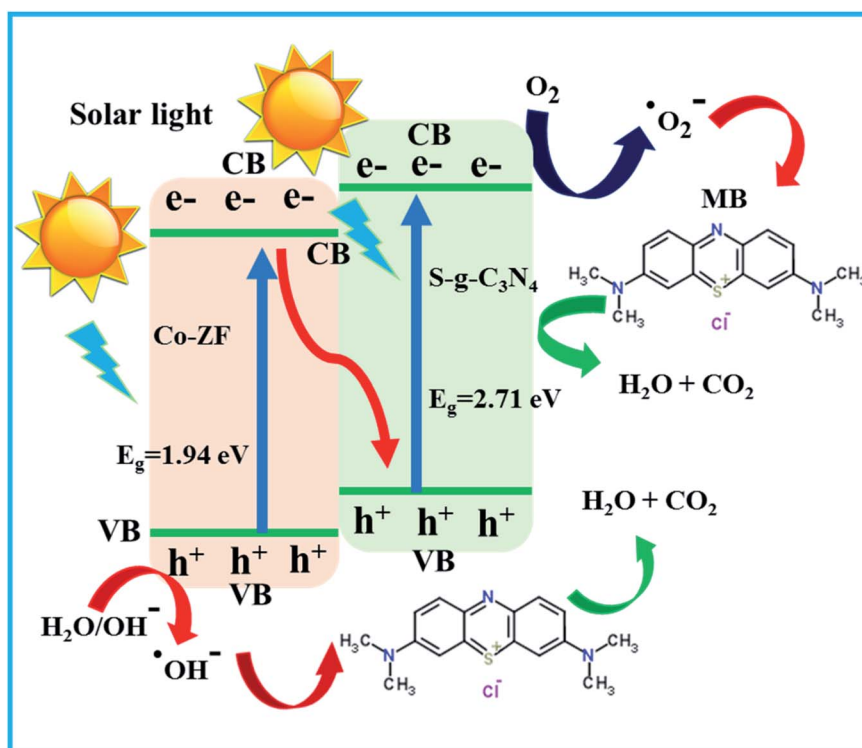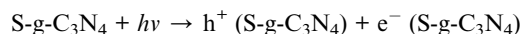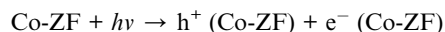

Fig. 6 Designing the reaction pathways for the photocatalytic elimination of MB using 48% S-g-C$_3$N$_4$/6% Co-ZF utilizing a feasible S-scheme heterojunction.
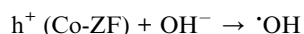
trapping experiment. This demonstrated that the primary energy species involved in the catalytic dye degradation process are $\cdot OH$ and $\cdot O_2^-$. Examining the EPR spectra of 48% S-g-C$_3$N$_4$/6% Co-ZF served as additional proof that functional species $\cdot OH$ and $\cdot O_2^-$ were present in the photodegradation process (Fig. S2a and b†). However, the signals are not discernible in the dark, indicating that both $\cdot O_2^-$ and $\cdot OH$ are constructed through the photolysis reaction practices. The apparent ESR signals are associated with $DMPO^-\cdot O_2^-$ and $DMPO^-\cdot OH$ adducts under sunlight enlightenment. The EPR results not only show that the 48% S-g-C$_3$N$_4$/6% Co-ZF heterojunction is produced, but they also show how effective the self-assembled method of S-g-C$_3$N$_4$/Co-ZF construction is for pollutant degradation. Fig. 6 shows a schematic representation of a photocatalytic process in the S-scheme under visible light. The MB dye degradation mechanism with the help of 48% S-g-C$_3$N$_4$/6% Co-ZF photocatalyst is shown in eqn (I)–(IV).

The adsorption of MB dye on 48% S-g-C$_3$N$_4$/6% Co-ZF photocatalyst surface and the e^-/h^+ pair contribute a significant role in MB degradation. Firstly, the MB molecule was adsorbed on the 48% S-g-C$_3$N$_4$/6% Co-ZF photocatalyst surface. On the illumination of solar light on the S-g-C$_3$N$_4$/6% Co-ZF photocatalyst generate e^-/h^+ pairs. Band gap alignment of Co-ZF with S-g-C$_3$N$_4$ minimizes the e^-/h^+ recombination. The holes in the lowest energy state in the conduction band of Co-ZF oxidized the MB dye directly and generate hydroxyl free radicals by reacting with water molecules which further interact with MB dye to oxidize into valuable products. Similarly, electrons in the highest energy state in the valence band of S-g-C$_3$N$_4$ reduce the adsorbed MB dye into CO$_2$. The degradation of MB is started by either $\cdot OH$ radicals, $\cdot O_2^-$ radicals, or direct transfer of holes. A detailed illustration of the photocatalytic mechanism is written below.
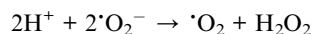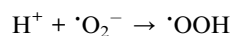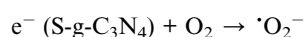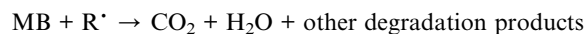
(I) Formation of electron–hole pair

$$Co\text{-}ZF + h\nu \rightarrow h^+ (Co\text{-}ZF) + e^- (Co\text{-}ZF)$$

$$S\text{-}g\text{-}C_3N_4 + h\nu \rightarrow h^+ (S\text{-}g\text{-}C_3N_4) + e^- (S\text{-}g\text{-}C_3N_4)$$

(II) Formation of $\cdot OH$ radical

$$e^- (S\text{-}g\text{-}C_3N_4) + H_2O_2 \rightarrow \cdot OH + OH^-$$

$$h^+ (Co\text{-}ZF) + H_2O \rightarrow \cdot OH + H^+$$

$$h^+ (Co\text{-}ZF) + OH^- \rightarrow \cdot OH$$

(III) Generation of other reactive species

$$e^- (S\text{-}g\text{-}C_3N_4) + O_2 \rightarrow \cdot O_2^-$$

$$H^+ + \cdot O_2^- \rightarrow \cdot OOH$$

$$2H^+ + 2\cdot O_2^- \rightarrow \cdot O_2 + H_2O_2$$

(IV) MB degradation mechanism

$$MB + R\cdot \rightarrow CO_2 + H_2O + \text{other degradation products}$$

where $R\cdot = \cdot OH$, $\cdot OOH$, h^+ (Co-ZF), e^- (S-g-C$_3$N$_4$), $\cdot O_2^-$, $\cdot O_2$.

Conclusion

In a nutshell, the goal of the current work was to create a better nanocomposite system by integrating S-g-C$_3$N$_4$ with a sunlight-sensitive photocatalyst with narrow bandgap, Co-ZF, to enhance the photo-responsive window of the material and, in turn, the photo-removal proficiency. The hydrothermal technique was successfully used to create the binary S-g-C$_3$N$_4$/Co-ZF photocatalysts. Additionally, the Co-ZF on S-g-C$_3$N$_4$ were consistently loaded after their first manufacture. Both binary and individual photocatalysts were used to break down MB in water. It was discovered that the binary S-g-C$_3$N$_4$/Co-ZF NCs considerably improved the photo-removal of MB and sunshine harvesting. The ideal loading is 48 wt% for the binary S-g-C$_3$N$_4$/Co-ZF NCs. The photolysis rate of dye is 0.42×10^{-3} min^{-1}, which is almost 2.45 times more than that of the individual photocatalysts (ZF, S-g-C$_3$N$_4$ and Co-ZF), and Co-ZF demonstrated the greatest photo-removal efficiency with a 98% efficiency. Additionally, the chemical stability experiment of the sample with a 48% S-g-C$_3$N$_4$/6% Co-ZF content showed that the hybrid system is extremely robust and reusable. The current research made a ground-breaking suggestion for a brand-new synthesis method and a distinctive binary photo-catalyst that is active in the sunshine.

Author contributions

Ali Bahadur: conception, performed photocatalytic experiments, visualization of data, writing reviewing, and editing. Shahid Iqbal: design of study, performed major experimental works, writing-original draft preparation. Mohsin Javed: conception, design of study, writing-original draft preparation and critical revision, supervision. Syeda Saba Hassan: analysis and/or interpretation of data, performed FTIR analysis. Sohail Nadeem: material synthesis, visualization of data, writing reviewing, and editing. Ali Akbar: methodology, reviewed original manuscript, and critical revision. Rami M. Alzhrani: drafting the revised manuscript, performed XRD analysis and critical revision. Murefah Mana Al-Anazy: reviewed original manuscript, and critical revision. Eslam B. Elkaeed: visualization of data, reviewed the original manuscript and critical revision. Hala A. Ibrahium: analysis and/or interpretation of data, performed FTIR analysis. Ayesha Mohyuddin: conducted XRD analysis, acquisition of data, writing-original draft preparation.

Conflicts of interest

The authors declare no conflict of interest.

Acknowledgements

References

1 T.-B. Nguyen, P.-N.-T. Ho, C.-W. Chen, C. P. Huang, R.-a. Doong and C.-D. Dong, *Environ. Sci.: Nano*, 2022, **9**, 229–242.

2 X. Bai, T. Jia, X. Wang, S. Hou, D. Hao and N. Bingjie, *Catal. Sci. Technol.*, 2021, **11**, 5432–5447.

3 H. A. Abubshait, S. Iqbal, S. A. Abubshait, M. T. Alotaibi, N. Alwadai, N. Alfryyan, H. O. Alsaab, N. S. Awwad and H. A. Ibrahium, *RSC Adv.*, 2022, **12**, 3274–3286.

4 H. Mao, Q. Zhang, F. Cheng, Z. Feng, Y. Hua, S. Zuo, A. Cui and C. Yao, *Ind. Eng. Chem. Res.*, 2022, **61**, 8895–8907.

5 S. Iqbal, M. Javed, S. S. Hassan, S. Nadeem, A. Akbar, M. T. Alotaibi, R. M. Alzhrani, N. S. Awwad, H. A. Ibrahium and A. Mohyuddin, *Colloids Surf., A*, 2022, **636**, 128177.

6 K. Riaz, S. Nadeem, A. Chrouda, S. Iqbal, A. Mohyuddin, S. U. Hassan, M. Javed, A. BaQais, N. Tamam, K. Aroosh, A. Rauf, M. A. S. Abourehab, M. I. Jamil, E. B. Elkaeed, R. M. Alzhrani, N. S. Awwad and H. A. Ibrahium, *Colloids Surf., A*, 2022, **649**, 129332.

7 S. Nadeem, H. H. Khushi, M. Javed, S. Iqbal, H. O. Alsaab, N. S. Awwad, H. A. Ibrahium, T. Akhter, A. Rauf and H. Raza, *J. Mol. Struct.*, 2022, **1252**, 132191.

8 S. Iqbal, M. Javed, M. A. Qamar, A. Bahadur, M. Fayyaz, A. Akbar, H. O. Alsaab, N. S. Awwad and H. A. Ibrahium, *ChemistrySelect*, 2022, **7**, e202103694.

9 M. Fan, Y. Cheng, X. Peng, H. Zhang, J. Wu, H. Tang, B. Li and Y. Zong, *ACS Sustainable Chem. Eng.*, 2022, **10**, 7664–7676.

10 M. Javed, M. A. Qamar, S. Shahid, H. O. Alsaab and S. Asif, *RSC Adv.*, 2021, **11**, 37254–37267.

11 G. Sarp and E. Yilmaz, *ACS Omega*, 2022, **7**, 23223–23233.

12 M. Chandra, U. Guharoy and D. Pradhan, *ACS Appl. Mater. Interfaces*, 2022, **14**, 22122–22137.

13 A. Bahadur, S. Iqbal, H. O. Alsaab, N. S. Awwad and H. A. Ibrahium, *RSC Adv.*, 2021, **11**, 36518–36527.

14 S. Iqbal, A. Bahadur, M. Javed, O. Hakami, R. M. Irfan, Z. Ahmad, A. AlObaid, M. M. Al-Anazy, H. B. Baghdadi, H. S. M. Abd-Rabboh, T. I. Al-Muhimeed, G. Liu and M. Nawaz, *Mater. Sci. Eng., B*, 2021, **272**, 115320.

15 S. Iqbal, N. Ahmad, M. Javed, M. A. Qamar, A. Bahadur, S. Ali, Z. Ahmad, R. M. Irfan, G. Liu and M. B. Akbar, *J. Environ. Chem. Eng.*, 2021, **9**, 104919.

16 J. Ding, L. Song, X. Li, L. Chen, X. Li, J. Sun, X. Zhang, Y. Wang and X. Tian, *ACS Appl. Energy Mater.*, 2022, **5**, 8800–8811.

17 C. Wang, W. Shi, K. Zhu, X. Luan and P. Yang, *Langmuir*, 2022, **38**, 5934–5942.

18 U. Sahoo, S. Pattnayak, S. Choudhury, S. Padhiari, M. Tripathy and G. Hota, *Ind. Eng. Chem. Res.*, 2022, **61**, 9703–9716.

19 F. Chen, T. Ma, T. Zhang, Y. Zhang and H. Huang, *Adv. Mater.*, 2021, **33**, 2005256.

20 T. Chen, L. Liu, C. Hu and H. Huang, *Chin. J. Catal.*, 2021, **42**, 1413–1438.

21 W. Liu, D. Zhang, R. Wang, Z. Zhang and S. Qiu, *ACS Appl. Mater. Interfaces*, 2022, **14**, 31782–31791.

22 M. Jafarzadeh, *ACS Appl. Mater. Interfaces*, 2022, **14**, 24993–25024.

23 S. Iqbal, A. Bahadur, M. Javed, G. Liu, T. I. Al-Muhimeed, A. A. AlObaid, Z. Ahmad, K. Feng and D. Xiao, *J. Alloys Compd.*, 2022, **892**, 162012.

24 L.-Z. Wu, *Acta Phys.-Chim. Sin.*, 2020, **36**, 2004005.

25 S. Shen, J. Pan, W. Zhou, J. Tang, H. Ding, J. Wang, L. Chen, C.-T. Au and S.-F. Yin, 2020, **36**, 1905068.

26 Z. Jin, Y. Li and X. Hao, *Acta Phys.-Chim. Sin.*, 2021, **37**, 1912033.

27 L. Jia, X. Tan, T. Yu and J. Ye, *Energy Fuels*, 2022, DOI: 10.1021/acs.energyfuels.2c01137.

28 C. Coromelci, M. Neamtu, M. Ignat, P. Samoila, M. F. Zaltariov and M. Palamaru, *Ceram. Int.*, 2022, **48**, 4829–4840.

29 A. Aridi, D. Naoufal, H. El-Rassy and R. Awad, *Ceram. Int.*, 2022, DOI: 10.1016/j.ceramint.2022.07.046.

30 S. Iqbal, *Appl. Catal., B*, 2020, **274**, 119097.

31 H. A. Al-Shwaiman, C. Akshhayya, A. Syed, A. H. Bahkali, A. M. Elgorban, A. Das, R. S. Varma and S. S. Khan, *Mater. Chem. Phys.*, 2022, **279**, 125759.

32 S. Anwer, D. H. Anjum, S. Luo, Y. Abbas, B. Li, S. Iqbal and K. Liao, *Chem. Eng. J.*, 2021, **406**, 126827.

33 C. Akshhayya, M. K. Okla, A. M. Thomas, A. A. Al-ghamdi, M. A. Abdel-Maksoud, B. Almunqedhi, H. AbdElgawad, L. L. Raju and S. S. Khan, *Mater. Chem. Phys.*, 2022, **277**, 125464.

34 P. A. Vinosha, J. V. A. Vinsla, J. Madhavan, S. Devanesan, M. S. AlSalhi, M. Nicoletti and B. Xavier, *Environ. Res.*, 2022, **203**, 111913.

35 R. Rajini and A. C. Ferdinand, *Chem. Data Collect.*, 2022, **38**, 100825.

36 R. Muhammad Irfan, M. Hussain Tahir, M. Maqsood, Y. Lin, T. Bashir, S. Iqbal, J. Zhao, L. Gao and M. Haroon, *J. Catal.*, 2020, **390**, 196–205.

37 K. Patil, K. Jangam, S. Patange, S. Balgude, A. G. Al-Sehemi, H. Pawar and P. More, *J. Phys. Chem. Solids*, 2022, **167**, 110783.

38 R. Belakehal, K. Atacan, N. Güy, A. Megriche and M. Özacar, *Appl. Surf. Sci.*, 2022, 154315, DOI: 10.1016/j.apsusc.2022.154315.

39 X. Jiang, Z. Wang, M. Zhang, M. Wang, R. Wu, X. Shi, B. Luo, D. Zhang, X. Pu and H. Li, *J. Alloys Compd.*, 2022, **912**, 165185.

40 H. B. Truong, B. T. Huy, S. K. Ray, G. Gyawali, Y.-I. Lee, J. Cho and J. Hur, *Chemosphere*, 2022, **299**, 134320.

41 B. Al-Najar, A. Younis, L. Hazeem, S. Sehar, S. Rashdan, M. N. Shaikh, H. Albuflasa and N. P. Hankins, *Chemosphere*, 2022, **288**, 132525.

42 S. Choudhary, D. Hasina, M. Saini, M. Ranjan and S. Mohapatra, *J. Alloys Compd.*, 2022, **895**, 162723.

43 G. Fan, Z. Gu, L. Yang and F. Li, *Chem. Eng. J.*, 2009, **155**, 534–541.

44 Y. Sun, W. Wang, L. Zhang, S. Sun and E. Gao, *Mater. Lett.*, 2013, **98**, 124–127.

45 L. Han, X. Zhou, L. Wan, Y. Deng and S. Zhan, *J. Environ. Chem. Eng.*, 2014, **2**, 123–130.

46 Y. Shi, L. Li, Z. Xu, H. Sun, S. Amin, F. Guo, W. Shi and Y. Li, *Mater. Res. Bull.*, 2022, **150**, 111789.

47 Y. Fang, Q. Liang, Y. Li and H. Luo, *Chemosphere*, 2022, **302**, 134832.

48 S. Gao, D. Feng, F. Chen, H. Shi and Z. Chen, *Colloids Surf., A*, 2022, **648**, 129282.

49 H.-Y. He, Y. Yan, J.-F. Huang and J. Lu, *Sep. Purif. Technol.*, 2014, **136**, 36–41.

50 S. Renukadevi and A. P. Jeyakumari, *Inorg. Chem. Commun.*, 2020, **118**, 108047.

51 J. Ai, L. Hu, Z. Zhou, L. Cheng, W. Liu, K. Su, R. Zhang, Z. Chen and W. Li, *Ceram. Int.*, 2020, **46**, 11786–11798.

52 X. Zhang, B. Lin, X. Li, X. Wang, K. Huang and Z. Chen, *Chem. Eng. J.*, 2022, **430**, 132728.

53 S. Khosravi-Gandomani, R. Yousefi, F. Jamali-Sheini and N. M. Huang, *Ceram. Int.*, 2014, **40**, 7957–7963.

54 Z. Zhu, F. Guo, Z. Xu, X. Di and Q. Zhang, *RSC Adv.*, 2020, **10**, 11929–11938.

55 S.-W. Zhao, M. Zheng, H.-L. Sun, S.-J. Li, Q.-J. Pan and Y.-R. Guo, *Dalton Trans.*, 2020, **49**, 3723–3734.

56 M. F. Abdel Messih, M. A. Ahmed, A. Soltan and S. S. Anis, *J. Phys. Chem. Solids*, 2019, **135**, 109086.

57 S. Iqbal, N. Ahmad, M. Javed, M. A. Qamar, A. Bahadur, S. Ali, Z. Ahmad, R. M. Irfan, G. Liu, M. B. Akbar and M. A. Qayyum, *J. Environ. Chem. Eng.*, 2021, **9**, 104919.

58 S. Iqbal, A. Bahadur, S. Ali, Z. Ahmad, M. Javed, R. M. Irfan, N. Ahmad, M. A. Qamar, G. Liu, M. B. Akbar and M. Nawaz, *J. Alloys Compd.*, 2021, **858**, 158338.

59 F. Khurshid, M. Jeyavelan, M. S. L. Hudson and S. Nagarajan, *R. Soc. Open Sci.*, 2019, **6**, 181764.

60 K. S. Riaz, M. S. Nadeem, V. V. Chrouda, P. A. Iqbal, M. Alsawalha, T. Alomayri and B. Yuan, *Colloids Surf.*, 2021, 125835.

61 J. Feng, *ACS Appl. Mater. Interfaces*, 2017, **9**, 14103–14111.

62 Q. Sun, K. Wu, J. Zhang and J. Sheng, *Nanotechnology*, 2019, **30**, 315706.

63 J. Wang, Q. Zhang, F. Deng, X. Luo and D. D. Dionysiou, *Chem. Eng. J.*, 2020, **379**, 122264.

64 G. J. Rani, K. J. Babu, G. G. Kumar and M. A. J. Rajan, *J. Alloys Compd.*, 2016, **688**, 500–512.

65 M. M. Sabzehmeidani, H. Karimi, M. Ghaedi and V. M. Avargani, *Mater. Res. Bull.*, 2021, **143**, 111449.